

# A Chebyshev-based High-order-accurate Integral Equation Solver for Maxwells Equations

Jin Hu, *Student Member, IEEE* and Constantine Sideris, *Member, IEEE*

**Abstract**—This paper introduces a new method for discretizing and solving integral equation formulations of Maxwell's equations which achieves spectral accuracy for smooth surfaces. The approach is based on a hybrid Nyström-collocation method using Chebyshev polynomials to expand the unknown current densities over curvilinear quadrilateral surface patches. As an example, the proposed strategy is applied to Magnetic Field Integral Equation (MFIE) and the N-Müller formulation for scattering from metallic and dielectric objects respectively. The convergence is studied for several different geometries, including spheres, cubes, and complex NURBS geometries imported from CAD software, and the results are compared against a commercial Method-of-Moments solver using RWG basis functions.

**Index Terms**—Integral equations, high-order accuracy, N-Müller formulation, spectral methods, scattering.

## I. INTRODUCTION

**D**UE to the lack of analytical solutions for anything but the simplest problems [1], efficient and accurate numerical methods for solving Maxwell's equations are crucial for a plethora of engineering applications today, including antennas, microwave devices, and nanophotonic structures. A recent resurgence in inverse design approaches [2], which involve the automated design of novel electromagnetic structures given a set of desired performance metrics and design constraints and require accurate field and gradient information at each iteration, further highlights the need for fast Maxwell solvers. Although finite difference [3] and finite element methods [4] are popular approaches due to their relative ease of implementation, they suffer from several major drawbacks: poor convergence due to finite difference approximations or low-order basis functions, significant numerical dispersion due to relying on local discrete differentiation, and they are often impractical for large problems due to their volumetric nature. On the other hand, boundary integral equation (BIE) formulations have been shown to be very effective in situations containing scatterers with small surface area to volume ratios due to only solving for unknowns on surfaces rather than volumes. Recently, BIEs have been successfully applied towards the modeling and optimization of nanophotonic devices in two dimensions, showing significant improvements in speed and accuracy over finite difference based methods [5]. The majority of present day implementations of BIE methods rely on discretization of objects via flat triangular discretizations, expanding unknown surface current densities with Rao-Wilton-Glisson (RWG)

basis functions, and utilizing the Method of Moments (MoM) for solving the resulting integral formulation [6]. Unfortunately, RWG functions are first order and cannot accurately approximate complex surface current distributions without very fine meshing. This often leads to poor convergence and conditioning of these implementations and significant research effort has gone into selecting alternative basis functions for testing or expansion in an attempt to improve performance [7]. [8] presented an alternative approach which achieves high-order accuracy by utilizing a Nyström method and discretizing the integrals on the basis of local coordinate charts together with fixed and floating partitions of unity. While effective, the approach of [8] relies on overlapping parameterized patches which can both increase the number of unknowns as well as significantly complicate the generation of surface meshes. Recently, [9] demonstrated a new high-order solution strategy for acoustic scattering problems based on non-overlapping parametric curvilinear patches. The method presented in [9] discretizes the unknowns on each patch on a Chebyshev grid, approximating the unknown surface densities using Chebyshev polynomials. A spectrally accurate Fejér quadrature rule is used for evaluating far interactions, and a Cartesian change of variables is used to cancel the singularity of the integrals associated with local and near interactions, leading to high-order accuracy in the numerical evaluation of both the singular and near-singular integrals.

In this work, we extend the methods presented in [9] for the scalar Helmholtz equation to the numerical solution of the fully-vectorial Maxwell case. In order to demonstrate the generality of the approach, we consider scattering from both Perfect Electrical Conductor (PEC) and dielectric objects. We focus on the solution of the MFIE formulation [10] for metallic objects and the N-Müller formulation [11] for dielectric objects due to their superior conditioning properties, although we remark that all of the methods presented in this work can readily be extended to the Electric and Combined Field Integral Equations (EFIE/CFIE) and other integral equation formulations designed for dielectric objects, such as the Poggio-Chang-Miller-Harrington-Wu-Tsai (PCMHW) formulation [12]. This paper is organized as follows. In Section II, we briefly review the MFIE and the N-Müller formulations. In Section III, we present the proposed high-order-accurate Chebyshev-based Boundary Integral Equation (CBIE) approach for discretizing the integral formulations. Finally, numerical results are presented in Section IV which evaluate the performance of the CBIE method by comparing the numerical solutions of plane-wave scattering from a PEC/dielectric sphere against analytical Mie-series solutions, as well as solving a PEC/dielectric cube for which no closed-

This authors gratefully acknowledge support by the National Science Foundation (1849965) and the Air Force Office of Scientific Research (FA9550-20-1-0087).

J. Hu and C. Sideris are with the Department of Electrical and Computer Engineering, University of Southern California, Los Angeles, CA 90089, USA (e-mails: jinhu@usc.edu, csideris@usc.edu).

form solutions exist. The accuracy is also compared against a commercial RWG-based MoM solver. Finally, we present results for scattering from two complex NURBS parametrized geometries generated by commercial CAD software.

## II. INTEGRAL EQUATION FORMULATIONS

### A. Magnetic Field Integral Equation Formulation for Closed Metallic Scatterers

We consider the problem of computing the scattered electric and magnetic fields  $(\mathbf{E}^{\text{scat}}, \mathbf{H}^{\text{scat}})$  that result due to an incident field excitation  $(\mathbf{E}^{\text{inc}}, \mathbf{H}^{\text{inc}})$  impinging on the surface  $\Gamma$  of a closed perfect metallic object  $D$  as illustrated in Fig. 1(a). Based on the Stratton-Chu formulas [13], Electric and Magnetic Field Integral Equations (EFIE/MFIE) can be derived which express the scattered electric and magnetic fields in terms of the physical current  $\mathbf{J} = \hat{\mathbf{n}} \times \mathbf{H}$  on the surface of a perfect metallic conducting object. Although either the EFIE, the MFIE, or a linear combination of the two can be used to solve for the scattered fields due to an incident excitation, only the MFIE is considered in this work due to its superior conditioning properties as a result of the nature of Fredholm integral equations of the second kind [13]. The classical MFIE can be expressed as,

$$\frac{\mathbf{J}}{2} + \mathcal{K}\mathbf{J} = \hat{\mathbf{n}} \times \mathbf{H}^{\text{inc}} \quad (1)$$

where  $\mathcal{K}$  is the operator:

$$\mathcal{K}[\mathbf{a}](\mathbf{r}) = \hat{\mathbf{n}}(\mathbf{r}) \times \int_{\Gamma} \mathbf{a}(\mathbf{r}') \times \nabla G(\mathbf{r} - \mathbf{r}') d\sigma(\mathbf{r}') \quad (2)$$

Note that  $\nabla$  denotes the gradient with respect to the coordinates of observation points  $\mathbf{r}$ ,  $G$  corresponds to the free space scalar Green's function:  $G(\mathbf{r} - \mathbf{r}') = \frac{\exp(-jk|\mathbf{r} - \mathbf{r}'|)}{4\pi|\mathbf{r} - \mathbf{r}'|}$  with wavenumber  $k = 2\pi/\lambda$ , and  $\hat{\mathbf{n}}$  denotes the outwardly pointing surface normal.

### B. N-Müller Formulation for Dielectric Scatterers

The second scenario that we consider is scattering from a penetrable dielectric object  $D$  with a permittivity  $\epsilon_d$  and a permeability  $\mu_d$  embedded in a homogeneous background medium characterized by permittivity  $\epsilon_e$  and permeability  $\mu_e$  in the presence of an incident field excitation  $(\mathbf{E}^{\text{inc}}, \mathbf{H}^{\text{inc}})$ . As shown in Fig. 1(b), since the object is now penetrable, the incident fields lead to scattered fields outside the object,  $(\mathbf{E}^{\text{scat}}, \mathbf{H}^{\text{scat}})$ , as well as transmitted fields inside,  $(\mathbf{E}^{\text{t}}, \mathbf{H}^{\text{t}})$ . Equivalent electric and magnetic current densities can then be defined based on the boundary tangential magnetic and electric fields respectively across the dielectric interface as:  $\mathbf{J} = \hat{\mathbf{n}} \times (\mathbf{H}^{\text{inc}} + \mathbf{H}^{\text{scat}}) = \hat{\mathbf{n}} \times \mathbf{H}^{\text{t}}$  and  $\mathbf{M} = (\mathbf{E}^{\text{inc}} + \mathbf{E}^{\text{scat}}) \times \hat{\mathbf{n}} = \mathbf{E}^{\text{t}} \times \hat{\mathbf{n}}$  on the surface  $\Gamma$  of  $D$ . By invoking the Stratton-Chu formula for the electric and magnetic fields outside of the object and crossing with the normal vector  $\hat{\mathbf{n}}$ , we obtain:

$$\frac{\mathbf{M}}{2} + \mathcal{K}_e \mathbf{M} - \eta_e \mathcal{T}_e \mathbf{J} = -\hat{\mathbf{n}} \times \mathbf{E}^{\text{inc}} \quad (3)$$

$$\frac{\mathbf{J}}{2} + \mathcal{K}_e \mathbf{J} + \frac{1}{\eta_e} \mathcal{T}_e \mathbf{M} = \hat{\mathbf{n}} \times \mathbf{H}^{\text{inc}} \quad (4)$$

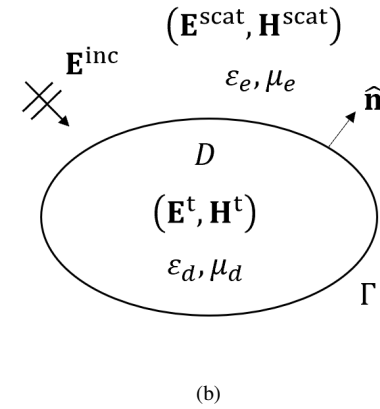
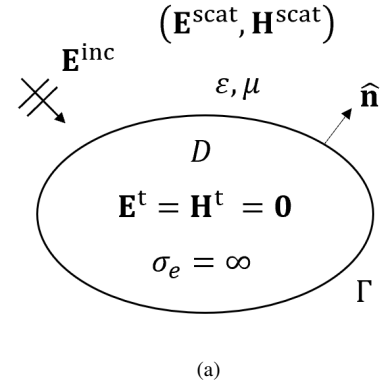


Fig. 1: (a) EM scattering from a closed PEC object. (b) EM scattering from a closed penetrable dielectric object.

where the  $\mathcal{K}_e$  and  $\mathcal{T}_e$  operators are defined as:

$$\mathcal{K}_e[\mathbf{a}](\mathbf{r}) = \hat{\mathbf{n}}(\mathbf{r}) \times \int_{\Gamma} \mathbf{a}(\mathbf{r}') \times \nabla G_e(\mathbf{r} - \mathbf{r}') d\sigma(\mathbf{r}') \quad (5)$$

$$\mathcal{T}_e[\mathbf{a}](\mathbf{r}) = \mathcal{T}_e^s[\mathbf{a}](\mathbf{r}) + \mathcal{T}_e^h[\mathbf{a}](\mathbf{r}) \quad (6)$$

$$\mathcal{T}_e^s[\mathbf{a}](\mathbf{r}) = jk_e \hat{\mathbf{n}}(\mathbf{r}) \times \int_{\Gamma} \mathbf{a}(\mathbf{r}') G_e(\mathbf{r} - \mathbf{r}') d\sigma(\mathbf{r}') \quad (7)$$

$$\mathcal{T}_e^h[\mathbf{a}](\mathbf{r}) = \frac{j}{k_e} \hat{\mathbf{n}}(\mathbf{r}) \times \int_{\Gamma} \nabla G_e(\mathbf{r} - \mathbf{r}') \nabla'_s \cdot \mathbf{a}(\mathbf{r}') d\sigma(\mathbf{r}') \quad (8)$$

where the subscript “e” in the operators indicates the exterior medium, which has wavenumber:  $k_e = 2\pi/\lambda_e$  and impedance:  $\eta_e = \sqrt{\mu_e/\epsilon_e}$ .

Similarly, another set of integral equations can be obtained for the transmitted fields  $(\mathbf{E}^{\text{t}}, \mathbf{H}^{\text{t}})$  inside the object:

$$\frac{\mathbf{M}}{2} - \mathcal{K}_d \mathbf{M} + \eta_d \mathcal{T}_d \mathbf{J} = \mathbf{0} \quad (9)$$

$$\frac{\mathbf{J}}{2} - \mathcal{K}_d \mathbf{J} - \frac{1}{\eta_d} \mathcal{T}_d \mathbf{M} = \mathbf{0} \quad (10)$$

where the  $\mathcal{K}_d$  and  $\mathcal{T}_d$  operators are defined in the same manner as  $\mathcal{K}_e$  and  $\mathcal{K}_d$ , except the “d” denotes the interior medium with corresponding wavenumber:  $k_d = 2\pi/\lambda_d$  and impedance:  $\eta_d = \sqrt{\mu_d/\epsilon_d}$

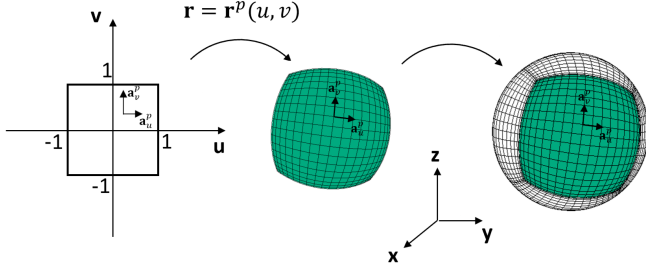


Fig. 2: The mapping from square  $[-1,1] \times [-1,1]$  in parameter domain to a patch on a sphere in Cartesian coordinates.

(3), (4), (9), and (10) give four equations for two unknowns ( $\mathbf{J}, \mathbf{M}$ ). They can be linearly combined as follows to reduce the system to two independent equations:

$$\begin{aligned} \alpha_1(3) + \alpha_2(9) \\ \beta_1(4) + \beta_2(10) \end{aligned} \quad (11)$$

Choosing  $\alpha_1 = \epsilon_e, \alpha_2 = \epsilon_d, \beta_1 = \mu_e, \beta_2 = \mu_d$  results in the classical N-Müller formulation, which has the advantage that it completely cancels the singular terms arising from the gradient of the Green's function in the  $\mathcal{T}_e^h$  and  $\mathcal{T}_d^h$  operators [14]. The combined system in matrix form is thus:

$$\begin{bmatrix} \epsilon_e \mathcal{K}_e - \epsilon_d \mathcal{K}_d + \frac{\epsilon_e + \epsilon_d}{2} \mathcal{I} & -(\mathcal{M}\mathcal{T}^s + \mathcal{M}\mathcal{T}^h) \\ \mathcal{M}\mathcal{T}^s + \mathcal{M}\mathcal{T}^h & \mu_e \mathcal{K}_e - \mu_d \mathcal{K}_d + \frac{\mu_e + \mu_d}{2} \mathcal{I} \end{bmatrix} \begin{bmatrix} \mathbf{M} \\ \mathbf{J} \end{bmatrix} = \begin{bmatrix} -\epsilon_e \hat{\mathbf{n}} \times \mathbf{E}^{\text{inc}} \\ \mu_e \hat{\mathbf{n}} \times \mathbf{H}^{\text{inc}} \end{bmatrix} \quad (12)$$

where  $\mathcal{I}$  is the identity operator,  $\mathcal{M}\mathcal{T}^s$  and  $\mathcal{M}\mathcal{T}^h$  are defined as

$$\begin{aligned} \mathcal{M}\mathcal{T}^s[\mathbf{a}](\mathbf{r}) &= (\sqrt{\mu_e \epsilon_e} \mathcal{T}_e^s - \sqrt{\mu_d \epsilon_d} \mathcal{T}_d^s)[\mathbf{a}](\mathbf{r}) \\ &= \frac{j}{\omega} \hat{\mathbf{n}}(\mathbf{r}) \times \int_{\Gamma} \mathbf{a}(\mathbf{r}') (k_e^2 G_e - k_d^2 G_d) d\sigma(\mathbf{r}') \end{aligned} \quad (13)$$

$$\begin{aligned} \mathcal{M}\mathcal{T}^h[\mathbf{a}](\mathbf{r}) &= (\sqrt{\mu_e \epsilon_e} \mathcal{T}_e^h - \sqrt{\mu_d \epsilon_d} \mathcal{T}_d^h)[\mathbf{a}](\mathbf{r}) \\ &= \frac{j}{\omega} \hat{\mathbf{n}}(\mathbf{r}) \times \int_{\Gamma} (\nabla G_e - \nabla G_d) \nabla'_s \cdot \mathbf{a}(\mathbf{r}') d\sigma(\mathbf{r}') \end{aligned} \quad (14)$$

The difference of the hypersingular operators  $\mathcal{T}^h$ ,  $\mathcal{M}\mathcal{T}^h$  does not have any singularity due to exact cancellation of the singular terms.

### III. CHEBYSHEV-BASED BOUNDARY INTEGRAL EQUATION APPROACH

#### A. Representation of Geometries/Densities

In order to solve (1) or (12), the surface  $\Gamma$  is first divided into a number ( $M$ ) of non-overlapping curvilinear patches  $\Gamma_p, p = 1, 2, \dots, M$ . We opt to use parametric curvilinear patches, rather than a more common flat triangular discretization, due to their ability to accurately represent curved surfaces with coarse discretizations. For each of these patches, a  $UV$  mapping is used to map from the standard  $[-1, 1] \times [1, 1]$  square in  $UV$  space to the corresponding parameterized surface in Cartesian coordinates as illustrated in Fig. 2. Defining the position vector on  $\Gamma_p$  as  $\mathbf{r} = \mathbf{r}^p(u, v) = (x^p(u, v), y^p(u, v), z^p(u, v))$ , we can

define the tangential covariant basis vectors and surface normal on  $\Gamma_p$  as

$$\mathbf{a}_u^p = \frac{\partial \mathbf{r}^p(u, v)}{\partial u}, \quad \mathbf{a}_v^p = \frac{\partial \mathbf{r}^p(u, v)}{\partial v}, \quad \hat{\mathbf{n}}^p = \frac{\mathbf{a}_u^p \times \mathbf{a}_v^p}{\|\mathbf{a}_u^p \times \mathbf{a}_v^p\|} \quad (15)$$

Thus, the vector triplet  $(\mathbf{a}_u^p, \mathbf{a}_v^p, \hat{\mathbf{n}}^p)$  forms a local conformal reference frame at each point on  $\Gamma_p$ . The metric tensor is defined as

$$G^p = \begin{bmatrix} g_{uu}^p & g_{uv}^p \\ g_{vu}^p & g_{vv}^p \end{bmatrix} \quad (16)$$

where  $g_{ij}^p = \mathbf{a}_i^p \cdot \mathbf{a}_j^p$  and thus we have surface element  $ds = \sqrt{|G^p|} du dv$  on  $\Gamma_p$  where  $|G^p|$  is the determinant of  $G^p$ . We can now represent the surface current density on  $\Gamma_p$  as

$$\begin{aligned} \mathbf{J}(\mathbf{r}^p(u, v)) &= \mathbf{J}^p(u, v) \\ &= \frac{1}{\sqrt{|G^p(u, v)|}} (J^{p,u}(u, v) \mathbf{a}_u^p(u, v) + J^{p,v}(u, v) \mathbf{a}_v^p(u, v)) \end{aligned} \quad (17)$$

$$\begin{aligned} \mathbf{M}(\mathbf{r}^p(u, v)) &= \mathbf{M}^p(u, v) \\ &= \frac{1}{\sqrt{|G^p(u, v)|}} (M^{p,u}(u, v) \mathbf{a}_u^p(u, v) + M^{p,v}(u, v) \mathbf{a}_v^p(u, v)) \end{aligned} \quad (18)$$

for  $p = 1, \dots, M$ , where  $J^{p,u}$  (resp.  $M^{p,u}$ ) and  $J^{p,v}$  (resp.  $M^{p,v}$ ) are scalar functions representing the contravariant components of the surface current density  $\mathbf{J}$  (resp.  $\mathbf{M}$ ) on the  $p^{\text{th}}$  patch normalized by the metric tensor,  $\sqrt{|G^p|}$ . The densities are normalized by the surface element in order to simplify the numerical computation of their divergence (see [13, sec. 6.2.5]). Due to their desirable spectral convergence properties for approximating smooth functions, we utilize Chebyshev polynomials to discretize the surface current densities:

$$J^{p,a} = \sum_{m=0}^{N_v^p-1} \sum_{n=0}^{N_u^p-1} \gamma_{n,m}^{p,a} T_n(u) T_m(v), \quad \text{for } a = u, v \quad (19)$$

$$M^{p,a} = \sum_{m=0}^{N_v^p-1} \sum_{n=0}^{N_u^p-1} \zeta_{n,m}^{p,a} T_n(u) T_m(v), \quad \text{for } a = u, v \quad (20)$$

where the Chebyshev coefficients  $\gamma_{n,m}^{p,j}$  and  $\zeta_{n,m}^{p,j}$  can be computed from the values of the densities on Chebyshev nodes,

$$\gamma_{n,m}^{p,a} = \frac{\alpha_n \alpha_m}{N_u^p N_v^p} \sum_{k=0}^{N_v^p-1} \sum_{l=0}^{N_u^p-1} J^{p,a}(u_l, v_k) T_n(u_l) T_m(v_k), \quad (21)$$

$$\zeta_{n,m}^{p,a} = \frac{\alpha_n \alpha_m}{N_u^p N_v^p} \sum_{k=0}^{N_v^p-1} \sum_{l=0}^{N_u^p-1} M^{p,a}(u_l, v_k) T_n(u_l) T_m(v_k), \quad (22)$$

based on the discrete-orthogonality property of Chebyshev polynomials [15], where

$$\alpha_n = \begin{cases} 1, & n = 0 \\ 2, & n \neq 0 \end{cases} \quad (23)$$

Therefore, only the unknowns at the Chebyshev nodes (37) are required to represent the continuous scalar densities  $J^{p,a}$  and  $M^{p,a}$  over the whole patch  $\Gamma_p$ , where  $a$  can be either  $u$  or

$v$ . In our specific implementation, these unknowns are ordered in vector form as:

$$\mathcal{J}^p = \begin{pmatrix} J^{p,u}(u_0, v_0) \\ \vdots \\ J^{p,u}(u_{N_u^p-1}, v_{N_v^p-1}) \\ J^{p,v}(u_0, v_0) \\ \vdots \\ J^{p,v}(u_{N_u^p-1}, v_{N_v^p-1}) \end{pmatrix}, \quad (24)$$

$$\mathcal{M}^p = \begin{pmatrix} M^{p,u}(u_0, v_0) \\ \vdots \\ M^{p,u}(u_{N_u^p-1}, v_{N_v^p-1}) \\ M^{p,v}(u_0, v_0) \\ \vdots \\ M^{p,v}(u_{N_u^p-1}, v_{N_v^p-1}) \end{pmatrix}, \quad (25)$$

Here,  $(u_l, v_k), l = 0, 1, \dots, N_u^p - 1, k = 0, 1, \dots, N_v^p - 1$  are the Cartesian product of the Chebyshev nodes in the  $u$  and  $v$  direction as given in (37) for a discretization using  $N_u^p \cdot N_v^p$  points on  $\Gamma_p$ .

### B. Discretization of operators

We now turn our attention towards discretization of the  $\mathcal{K}/\mathcal{K}_e/\mathcal{K}_d$ ,  $\mathcal{MT}^s$  and  $\mathcal{MT}^h$  operators. We will begin by discretizing the  $\mathcal{K}$  operator first. Clearly, any integral over  $\Gamma$  can be split into the sum of integrals over each of the  $M$  patches,

$$\begin{aligned} \mathcal{K}[\mathbf{J}](\mathbf{r}) &= \sum_{p=1}^M \mathcal{K}[\mathbf{J}^p] \\ \mathcal{K}[\mathbf{J}^p](\mathbf{r}) &= \hat{\mathbf{n}}(\mathbf{r}) \times \int_{\Gamma^p} \mathbf{J}^p(\mathbf{r}') \times \nabla G(\mathbf{r} - \mathbf{r}') d\sigma(\mathbf{r}') \\ &= \hat{\mathbf{n}}(\mathbf{r}) \times \int_{-1}^1 \int_{-1}^1 (J^{p,u}(u, v) \mathbf{a}_u^p(u, v) + J^{p,v}(u, v) \mathbf{a}_v^p(u, v)) \\ &\quad \times \nabla G(\mathbf{r} - \mathbf{r}^p(u, v)) du dv \end{aligned} \quad (26)$$

Note that the  $\sqrt{|G^p(u, v)|}$  in the denominator of the expansion (17) for  $\mathbf{J}$  cancels with the Jacobian  $\sqrt{|G^p(u, v)|}$  that appears in the integral. In its current form, (26) contains the hyper-singular kernel  $\nabla G$ ; however, it can be manipulated using the BAC-CAB vector identity into

$$\begin{aligned} \mathcal{K}[\mathbf{J}^p](\mathbf{r}) &= \int_{-1}^1 \int_{-1}^1 J^{p,u}(u, v) (\mathbf{a}_u^p(u, v) \frac{\partial G(\mathbf{r} - \mathbf{r}^p(u, v))}{\partial \hat{\mathbf{n}}(\mathbf{r})} \\ &\quad - \nabla G(\mathbf{r} - \mathbf{r}^p(u, v)) \hat{\mathbf{n}}(\mathbf{r}) \cdot \mathbf{a}_u^p(u, v)) du dv + \\ &\quad \int_{-1}^1 \int_{-1}^1 J^{p,v}(u, v) (\mathbf{a}_v^p(u, v) \frac{\partial G(\mathbf{r} - \mathbf{r}^p(u, v))}{\partial \hat{\mathbf{n}}(\mathbf{r})} \\ &\quad - \nabla G(\mathbf{r} - \mathbf{r}^p(u, v)) \hat{\mathbf{n}}(\mathbf{r}) \cdot \mathbf{a}_v^p(u, v)) du dv \end{aligned} \quad (27)$$

which is weakly singular since  $\hat{\mathbf{n}}(\mathbf{r}) \cdot \mathbf{a}_{u,v}^p$  approaches 0 as  $\mathbf{r}^p(u, v) \rightarrow \mathbf{r}$ . Substituting (27) into (1), we must obtain  $N = 2 \sum_{p=1}^M N_u^p N_v^p$  linearly independent equations in order to obtain a uniquely solvable linear system for approximating  $\mathbf{J}$  on  $\Gamma$ . This is achieved by using a collocation method and testing (1) at same points as the unknowns. Since  $\mathbf{J}$  is a vector

function with two unknown contravariant components, we must test the MFIE at each point with two linearly independent vectors. The natural choice for this is the set of normalized covariant basis vectors  $\sqrt{G^p} \mathbf{a}^{p,u}$  and  $\sqrt{G^p} \mathbf{a}^{p,v}$  where the covariant basis vectors  $\mathbf{a}^{p,u}$  and  $\mathbf{a}^{p,v}$  are defined via the orthogonality relation

$$\mathbf{a}^{p,a} \cdot \mathbf{a}_b^p = \begin{cases} 1 & a = b \\ 0 & a \neq b \end{cases} \quad (28)$$

since dotting (1) with them results in expanding the right hand side  $\hat{\mathbf{n}} \times \mathbf{H}^{\text{inc}}$  using the basis vectors as the unknown densities. We can now define the linear system:

$$\begin{bmatrix} \frac{I}{2} + K^{11} & K^{12} & \dots & K^{1M} \\ K^{21} & \frac{I}{2} + K^{22} & \dots & K^{2M} \\ \vdots & \vdots & \ddots & \vdots \\ K^{M1} & K^{M2} & \dots & \frac{I}{2} + K^{MM} \end{bmatrix} \begin{bmatrix} \mathcal{J}^1 \\ \mathcal{J}^2 \\ \vdots \\ \mathcal{J}^M \end{bmatrix} = \begin{bmatrix} \mathcal{H}_{\text{inc}}^1 \\ \mathcal{H}_{\text{inc}}^2 \\ \vdots \\ \mathcal{H}_{\text{inc}}^M \end{bmatrix} \quad (29)$$

where

$$\mathcal{H}_{\text{inc}}^p = \begin{pmatrix} -\mathbf{a}_v^p \cdot \mathbf{H}^{p,\text{inc}}(u_0, v_0) \\ \vdots \\ -\mathbf{a}_v^p \cdot \mathbf{H}^{p,\text{inc}}(u_{N_u^p-1}, v_{N_v^p-1}) \\ \mathbf{a}_u^p \cdot \mathbf{H}^{p,\text{inc}}(u_0, v_0) \\ \vdots \\ \mathbf{a}_u^p \cdot \mathbf{H}^{p,\text{inc}}(u_{N_u^p-1}, v_{N_v^p-1}) \end{pmatrix} \quad (30)$$

represents the incident magnetic field on the  $p^{\text{th}}$  patch and  $\mathcal{J}^p, p = 1, 2, \dots, M$  is given in (24). Note the vector identities used in arriving at the expression in (30) are:

$$\begin{aligned} \sqrt{G^p} \mathbf{a}^{p,u} \cdot \hat{\mathbf{n}}^p \times \mathbf{H}^{p,\text{inc}} &= \mathbf{a}^{p,u} \cdot ((\mathbf{a}_u^p \times \mathbf{a}_v^p) \times \mathbf{H}^{p,\text{inc}}) \\ &= \mathbf{H}^{p,\text{inc}} \cdot (\mathbf{a}^{p,u} \times (\mathbf{a}_u^p \times \mathbf{a}_v^p)) \\ &= \mathbf{H}^{p,\text{inc}} \cdot (\mathbf{a}_u^p (\mathbf{a}^{p,u} \cdot \mathbf{a}_v^p) - \mathbf{a}_v^p (\mathbf{a}^{p,u} \cdot \mathbf{a}_u^p)) = -\mathbf{a}_v^p \cdot \mathbf{H}^{p,\text{inc}} \end{aligned} \quad (31)$$

Similarly,  $\sqrt{G^p} \mathbf{a}^{p,v} \cdot \hat{\mathbf{n}}^p \times \mathbf{H}^{p,\text{inc}} = \mathbf{a}_u^p \cdot \mathbf{H}^{p,\text{inc}}$ . Matrix block  $K^{qp}$  represents contributions of the appropriately discretized  $\mathcal{K}$  operator from the densities of the patch  $p$  to the target points on patch  $q$  and consists of the individual sub-blocks:

$$K^{qp} = \begin{pmatrix} K_{uu}^{qp} & K_{uv}^{qp} \\ K_{vu}^{qp} & K_{vv}^{qp} \end{pmatrix} \quad (32)$$

For the operators used in the N-Müller formulation, the matrix blocks corresponding to the  $\mathcal{K}_e$  and  $\mathcal{K}_d$  operator can be obtained in exactly the same way as  $\mathcal{K}$  operator by simply replacing the wavenumber  $k$  in the Green's function in (27) with  $k_e$  and  $k_d$  respectively. The integral of the  $\mathcal{MT}^s$  and  $\mathcal{MT}^h$  operators can also be split over each patch in as similar way as the  $\mathcal{K}$  operator:

$$\begin{aligned} \mathcal{MT}^s[\mathbf{J}](\mathbf{r}) &= \sum_{p=1}^M \mathcal{MT}^s[\mathbf{J}^p] \\ \mathcal{MT}^s[\mathbf{J}^p](\mathbf{r}) &= \frac{j}{\omega} \hat{\mathbf{n}}(\mathbf{r}) \times \int_{\Gamma^p} \mathbf{J}^p(\mathbf{r}') (k_e^2 G_e - k_d^2 G_d) d\sigma(\mathbf{r}') \\ &= \frac{j}{\omega} \hat{\mathbf{n}}(\mathbf{r}) \times \int_{-1}^1 \int_{-1}^1 (J^{p,u}(u, v) \mathbf{a}_u^p(u, v) + J^{p,v}(u, v) \mathbf{a}_v^p(u, v)) \\ &\quad (k_e^2 G_e(\mathbf{r} - \mathbf{r}^p(u, v)) - k_d^2 G_d(\mathbf{r} - \mathbf{r}^p(u, v))) du dv \end{aligned} \quad (33)$$



$$\begin{aligned}
\mathcal{MT}^h[\mathbf{J}](\mathbf{r}) &= \sum_{p=1}^M \mathcal{MT}^h[\mathbf{J}^p] \\
\mathcal{MT}^h[\mathbf{J}^p](\mathbf{r}) &= \frac{j}{\omega} \hat{\mathbf{n}}(\mathbf{r}) \times \int_{\Gamma^p} (\nabla G_e - \nabla G_d) \nabla'_s \cdot \mathbf{J}^p(\mathbf{r}') d\sigma(\mathbf{r}') \\
&= \frac{j}{\omega} \hat{\mathbf{n}}(\mathbf{r}) \times \int_{-1}^1 \int_{-1}^1 (\nabla G_e - \nabla G_d) \left( \frac{\partial J^{p,u}}{\partial u} + \frac{\partial J^{p,v}}{\partial v} \right) dudv \\
&= \frac{j}{\omega} \hat{\mathbf{n}}(\mathbf{r}) \times \int_{-1}^1 \int_{-1}^1 (\nabla G_e(\mathbf{r} - \mathbf{r}^p(u, v)) - \nabla G_d(\mathbf{r} - \mathbf{r}^p(u, v))) \\
&\quad \left( \sum_{m=0}^{N_v^p-1} \sum_{n=0}^{N_u^p-1} \gamma_{n,m}^{p,u} T'_n(u) T_m(v) + \sum_{m=0}^{N_v^p-1} \sum_{n=0}^{N_u^p-1} \gamma_{n,m}^{p,v} T_n(u) T'_m(v) \right) \\
&\quad dudv \\
&= \sum_{m=0}^{N_v^p-1} \sum_{n=0}^{N_u^p-1} \frac{j}{\omega} \hat{\mathbf{n}}(\mathbf{r}) \times \int_{-1}^1 \int_{-1}^1 (\gamma_{n,m}^{p,u} T'_n(u) T_m(v) + \\
&\quad \gamma_{n,m}^{p,v} T_n(u) T'_m(v)) (\nabla G_e(\mathbf{r} - \mathbf{r}^p(u, v)) - \nabla G_d(\mathbf{r} - \mathbf{r}^p(u, v))) \\
&\quad dudv
\end{aligned} \tag{34}$$

The partial derivative of the densities can be readily computed by taking the derivative of the corresponding Chebyshev polynomials. After the substitution of (33) and (34) into (12) with the expansion defined in (19) and (20), testing (12) at the same collocation points as the unknowns results in the linear system:

$$\begin{bmatrix} \epsilon_e K_e - \epsilon_d K_d + \frac{\epsilon_e + \epsilon_d}{2} I & -(MT^s + MT^h) \\ MT^s + MT^h & \mu_e K_e - \mu_d K_d + \frac{\mu_e + \mu_d}{2} I \end{bmatrix} \begin{bmatrix} \mathcal{M} \\ \mathcal{J} \end{bmatrix} = \begin{bmatrix} -\epsilon_e \mathcal{E}_{\text{inc}} \\ \mu_e \mathcal{H}_{\text{inc}} \end{bmatrix} \tag{35}$$

The block in  $\mathcal{E}_{\text{inc}}$  corresponding to the incident electric field on the  $p^{\text{th}}$  patch can be obtained in the same manner as in (31):

$$\mathcal{E}_{\text{inc}}^p = \begin{pmatrix} -\mathbf{a}_v^p \cdot \mathbf{E}^{p,\text{inc}}(u_0, v_0) \\ \vdots \\ -\mathbf{a}_v^p \cdot \mathbf{E}^{p,\text{inc}}(u_{N_u^p-1}, v_{N_v^p-1}) \\ \mathbf{a}_u^p \cdot \mathbf{E}^{p,\text{inc}}(u_0, v_0) \\ \vdots \\ \mathbf{a}_u^p \cdot \mathbf{E}^{p,\text{inc}}(u_{N_u^p-1}, v_{N_v^p-1}) \end{pmatrix} \tag{36}$$

The counterpart  $\mathcal{H}_{\text{inc}}^p$  is defined in (30). The matrices  $K_e$ ,  $K_d$ ,  $MT^s$  and  $MT^h$  all have the same block structure arranged by patches as indicated in (29) and (32) for the matrix  $K$ . A suitable numerical integration strategy must now be chosen for evaluating the necessary operators to compute the above matrix sub-blocks. In the following two subsections, we will detail our approach for dealing with the non-adjacent interactions ( $p \neq q$ ) and the singular and near-singular interactions arising either when  $p = q$  or when  $p \neq q$ , but the target point on  $q$  is located very near to the source patch  $p$ .

### C. Non-adjacent Interactions

The integrals (27), (33) and (34) are smooth for target points far away from the source patch  $p$ . Since the current density

$\mathbf{J}/\mathbf{M}$  is discretized on a Chebyshev grid on each patch, we can use Fejér's first quadrature rule to numerically evaluate these integrals with high-order accuracy. The quadrature nodes and weights for an order  $N$  open rule are given by:

$$x_i = \cos\left(\pi \frac{2i+1}{2N}\right), \quad i = 0, \dots, N-1 \tag{37}$$

$$w_i = \frac{2}{N} \left( 1 - 2 \sum_{k=1}^{N/2} \frac{1}{4k^2 - 1} \cos\left(k\pi \frac{2i+1}{N}\right) \right) \tag{38}$$

and the discretized versions of (27), (33) and (34) become (with  $a = \{u, v\}$  and  $b = \{u, v\}$ ):

$$K_{ba}^{qp}[J^{p,a}](u', v') = \sum_{k=0}^{N_v^p-1} \sum_{l=0}^{N_u^p-1} A_{ba}^{qp}(u', v', u_l, v_k) \tag{39}$$

$$\begin{aligned}
&\sqrt{|G^q(u', v')|} w_l w_k J^{p,a}(u_l, v_k) \\
MT_{ba}^{s,qp}[J^{p,a}](u', v') &= \sum_{k=0}^{N_v^p-1} \sum_{l=0}^{N_u^p-1} B_{ba}^{qp}(u', v', u_l, v_k) \\
&\sqrt{|G^q(u', v')|} w_l w_k J^{p,a}(u_l, v_k)
\end{aligned} \tag{40}$$

$$\begin{aligned}
MT_{ba}^{h,qp}[J^{p,a}](u', v') &= \sum_{k=0}^{N_v^p-1} \sum_{l=0}^{N_u^p-1} C_{ba}^{qp}(u', v', u_l, v_k) \\
&\sqrt{|G^q(u', v')|} w_l w_k \frac{\partial J^{p,a}}{\partial a}(u_l, v_k)
\end{aligned} \tag{41}$$

with

$$\begin{aligned}
A_{ba}^{qp}(u', v', u_l, v_k) &= \mathbf{a}^{q,b}(u', v') \cdot \mathbf{a}_a^p(u_l, v_k) \\
\frac{\partial G(\mathbf{r}^q(u', v') - \mathbf{r}^p(u_l, v_k))}{\partial \hat{\mathbf{n}}^q(u', v')} &- \hat{\mathbf{n}}^q(u', v') \cdot \mathbf{a}_a^p(u_l, v_k) \\
\mathbf{a}^{q,b}(u', v') \cdot \nabla G(\mathbf{r}^q(u', v') - \mathbf{r}^p(u_l, v_k))
\end{aligned} \tag{42}$$

$$\begin{aligned}
B_{ba}^{qp}(u', v', u_l, v_k) &= \frac{j}{\omega} \mathbf{a}^{q,b}(u', v') \cdot (\hat{\mathbf{n}}^q(u', v') \times \mathbf{a}_a^p(u_l, v_k)) \\
[k_e^2 G_e - k_d^2 G_d](\mathbf{r}^q(u', v') - \mathbf{r}^p(u_l, v_k))
\end{aligned} \tag{43}$$

$$\begin{aligned}
C_{ba}^{qp}(u', v', u_l, v_k) &= \frac{j}{\omega} \mathbf{a}^{q,b}(u', v') \cdot \hat{\mathbf{n}}^q(u', v') \times \\
&[\nabla G_e - \nabla G_d](\mathbf{r}^q(u', v') - \mathbf{r}^p(u_l, v_k))
\end{aligned} \tag{44}$$

where  $u_l$  and  $v_k$  are the discretization points on the Chebyshev grid corresponding to the  $x_i$  nodes:  $u_l = x_l | l = 0, \dots, N_u^p - 1$ ,  $v_k = x_k | k = 0, \dots, N_v^p - 1$ , and  $w_l$  and  $w_k$  are the quadrature weights in the  $u$  and  $v$  directions respectively.

### D. Singular and Near-singular Interactions

When the observation point  $(u', v')$  is on the same patch as the source patch  $p$ , the integrals (27), (33) and (34) become singular<sup>1</sup>. In order to accurately compute the resulting integrals with high-order accuracy we consider the following smoothing change of variables [16, Sec. 3.5]:

$$u(s) = \xi_{u'}(s), \quad v(t) = \xi_{v'}(t), \quad \text{for } -1 \leq s, t \leq 1 \tag{45}$$

<sup>1</sup>Actually, the integral (34) for  $MT^h$  remains regular due to the Müller cancellation and does not require special consideration; however, for simplicity we treat it in the same way as the other operators in our implementation.

where

$$\begin{aligned}\xi_\alpha(\tau) &= \begin{cases} \alpha + \left(\frac{\text{sgn}(\tau)-\alpha}{\pi}\right) w(\pi|\tau|), & \text{for } \alpha \neq \pm 1 \\ \alpha \mp \left(\frac{1\pm\alpha}{\pi}\right) w\left(\pi\left|\frac{\tau\mp 1}{2}\right|\right), & \text{for } \alpha = \pm 1 \end{cases} \\ w(\tau) &= 2\pi \frac{[\nu(\tau)]^d}{[\nu(\tau)]^d + [\nu(2\pi - \tau)]^d}, \quad 0 \leq \tau \leq 2\pi \\ \nu(\tau) &= \left(\frac{1}{d} - \frac{1}{2}\right) \left(\frac{\pi - \tau}{\pi}\right)^3 + \frac{1}{d} \left(\frac{\tau - \pi}{\pi}\right) + \frac{1}{2}\end{aligned}\quad (46)$$

The derivatives of  $w(\tau)$  vanish up to order  $d - 1$  at the endpoints, and therefore  $d - 1$  derivatives of  $\xi_\alpha(\tau)$  also vanish at  $\tau = 0$ , corresponding to  $\xi_\alpha(0) = \alpha$ . Now, since  $J^{p,a}(a = u, v)$  is expanded in terms of Chebyshev polynomials, which satisfy a discrete orthogonality property on the Chebyshev grid points, we can accurately precompute the action of the  $K_{ba}^{qp}$ ,  $\mathcal{MT}_{ba}^{s,qp}$  and  $\mathcal{MT}_{ba}^{h,qp}$  operators on each Chebyshev polynomial individually:

$$\begin{aligned}K_{ba}^{qp}[T_{mn}](u', v') &= \sum_{k=0}^{N_\beta^u-1} \sum_{l=0}^{N_\beta^v-1} A_{ba}^{qp}(u', v', \xi_{u'}(s_l), \xi_{v'}(t_k)) \\ \frac{\partial u}{\partial s}(s_l) \frac{\partial v}{\partial t}(t_k) w_l w_k T_{mn}(\xi_{u'}(s_l), \xi_{v'}(t_k))\end{aligned}\quad (47)$$

where  $\frac{\partial u}{\partial s} \rightarrow 0$  and  $\frac{\partial v}{\partial t} \rightarrow 0$  as  $\xi_{u'}(s) \rightarrow u'$  and  $\xi_{v'}(t) \rightarrow v'$  respectively, canceling the singularity in  $A$ . Note that the expressions for  $\mathcal{MT}_{ba}^{s,qp}$  and  $\mathcal{MT}_{ba}^{h,qp}$  are the same but with  $A$  replaced by  $B$  and  $C$  respectively. It is important that  $N_\beta^{u,v}$  is chosen sufficiently large to accurately compute each of the precomputation integrals in (47) above. A numerical analysis of the resulting forward map accuracy vs  $N_\beta^{u,v}$  is done in Section IV. Finally, on the basis of these precomputations, the action of each of these operators on any  $J^{p,a}$  or  $M^{p,a}$  can be readily computed using the Chebyshev expansion of the density, eg.

$$K_{ba}^{qp}[J^{p,a}](u', v') = \sum_{m=0}^{N_\beta^p-1} \sum_{n=0}^{N_\beta^a-1} \gamma_{m,n}^{p,a} K_{ba}^{qp}[T_{mn}](u', v')\quad (48)$$

where  $\gamma_{m,n}^{p,a}$  are the Chebyshev expansion coefficients defined in (19). An analogous relation also holds true for the  $\mathcal{MT}^s$  and  $\mathcal{MT}^h$  operators. This precomputation approach is also used in order to accurately compute the  $K_{ba}^{qp}$ ,  $\mathcal{MT}_{ba}^{s,qp}$  and  $\mathcal{MT}_{ba}^{h,qp}$  blocks corresponding to target points which are on different patches but which are still in close proximity to the source patch, making the integration near-singular. The only difference in this scenario arises in the selection of  $\alpha$  in the change of variable expression (46). Instead of simply choosing the  $(u', v')$  corresponding to the target point, since it is on a different patch, we search for:

$$(u^*, v^*) = \arg \min_{(u,v) \in [-1,1]^2} |\mathbf{r}^q(u', v') - \mathbf{r}^p(u, v)|\quad (49)$$

for the change-of-variables as the point on the source patch nearest to the target patch, which can be readily found by an appropriate minimization algorithm. We adopted the golden section search algorithm in our specific implementation [17].

## IV. NUMERICAL RESULTS

We first present the convergence of the forward map for both the MFIE and N-Müller formulations with respect to the order of expansion used ( $N$ ) for varying levels of singular integration refinement ( $N_\beta$ ). Following this, several numerical examples involving scattering from PEC and dielectric spheres and cubes are presented and compared against a commercial RWG-based MoM solver to demonstrate the high accuracy that can be achieved using the proposed CBIE method. Finally, we present scattering and near-field density results from scattering by highly intricate 3D NURBS objects parametrized with commercial CAD software [18], which shows that the approach can be readily applied to simulate objects arising in realistic applications.

### A. Forward Map Convergence

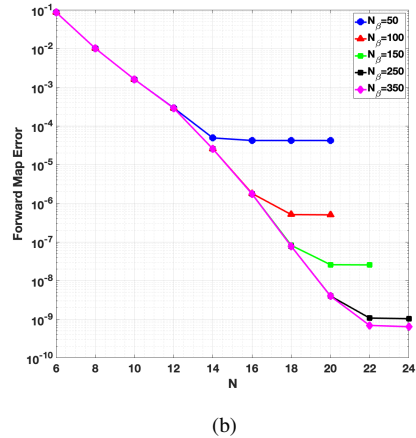
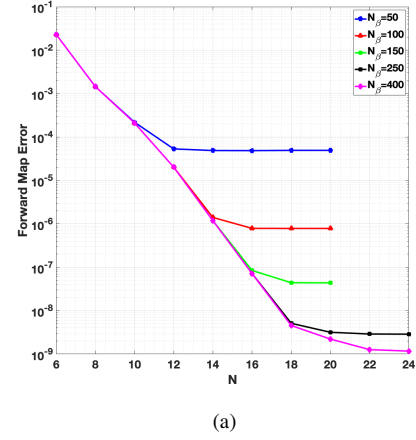


Fig. 3: (a) Forward mapping error with respect to  $N$  for various choices of  $N_\beta$  on a PEC sphere ( $D = 2\lambda$ ) using the MFIE formulation. (b) Forward mapping error on a dielectric sphere ( $D = 2\lambda_e, \epsilon_e = 1.0, \epsilon_d = 2.0$ ) using the N-Müller formulation.

Fig. 3 plots the forward mapping error (i.e., applying the integral operators to a reference solution and checking the accuracy of the result) on a  $2\lambda$  ( $2\lambda_e$ ) diameter sphere geometry for both the PEC and dielectric cases versus  $N$  for various

different choices of  $N_\beta$ . In the dielectric case, the exterior  $\epsilon_e = 1.0$  and the interior  $\epsilon_d = 2.0$ . The Mie series solution due to an incident plane wave is used as the reference solution [19]. As can be seen, depending on the desired accuracy, it is important to choose  $N_\beta$  judiciously such that it does not limit the overall solution accuracy. Increasing  $N_\beta$  does not increase the number of unknowns (controlled by  $N$ ); however, it can significantly increase the amount of time required to precompute the singular and near-singular interactions.

### B. PEC scattering: MFIE Formulation

In this subsection, we test the proposed approach for the MFIE formulation by computing scattered fields from three PEC objects: two spheres of diameters  $1.2\lambda$  and  $4\lambda$  and a cube with side length  $1.2\lambda$ . All three objects are parameterized by using 6 patches, and each patch is discretized with the same number of unknowns  $N = N_u = N_v$ . Thus the total number of unknowns per problem is  $Q = 2 \times 6 \times N^2$ . The spheres are illuminated by the same plane wave source,  $\mathbf{E}^{\text{inc}} = \exp(-ikz) \hat{\mathbf{x}}$ . Since a closed-form solution does not exist for scattering from a cube, we use an electric dipole excitation,  $\mathbf{H}^{\text{inc}}(\mathbf{r}) = -\nabla \times \{G(\mathbf{r}, \mathbf{r}') \mathbf{p}\}$ , placed at position  $\mathbf{r}' = (0.06\lambda, 0.06\lambda, 0.06\lambda)$  inside the cube with polarization  $\mathbf{p} = (1, 1, 1)$ . This allows us to determine convergence of the numerical solution since the scattered electric field must cancel the incident field outside the cube, and thus:  $\mathbf{H}^{\text{scat}}(\mathbf{r}) = \nabla \times \{G(\mathbf{r}, \mathbf{r}') \mathbf{p}\}$  ( $\mathbf{r} \in \mathcal{R}^3 \setminus D$ ). The results for the sphere cases are compared against the analytical Mie series solutions.

Fig. 4(a) shows the computed surface current density magnitude on the  $4\lambda$  sphere for  $N = 26$  and Fig. 4(b) shows the error difference in surface density between the computed and analytical solution on the  $4\lambda$  sphere for  $N = 26$ . As can be seen, the numerical solution differs from the exact solution by less than  $5.7 \times 10^{-7}$  at every point on the sphere. Fig. 4(c) plots the computed surface current distribution on the cube resulting from the internal dipole source. Fig. 5 plots the computed RCS overlaid on top of the analytical far-field solution of the  $4\lambda$  sphere for varying altitudes at  $\phi = 0^\circ$  and  $\phi = 90^\circ$ . The computed RCS points are indistinguishable from the analytical solution for both curves.

Fig. 6 plots the error of the CBIE method vs number of unknowns ( $Q$ ) used to discretize each scatterer. As a comparison, the convergence of a commercial MoM RWG-based solver for the  $4\lambda$  sphere case is also plotted. For reference, 1<sup>st</sup> and 12<sup>th</sup> order slopes are drawn in dashed lines. As can be seen, the MoM solver only approaches first order convergence, requires a much finer discretization than the proposed CBIE method, and even for a very high resolution mesh barely exceeds two digits of accuracy. In contrast, CBIE converges spectrally fast for all 3 examples, which makes it a significantly more accurate and efficient approach.

### C. Dielectric scattering: N-Müller formulation

The scattered fields from two dielectric objects are computed to evaluate the performance of the CBIE method for the N-Müller formulation: a dielectric sphere of  $2\lambda_e$  diameter with

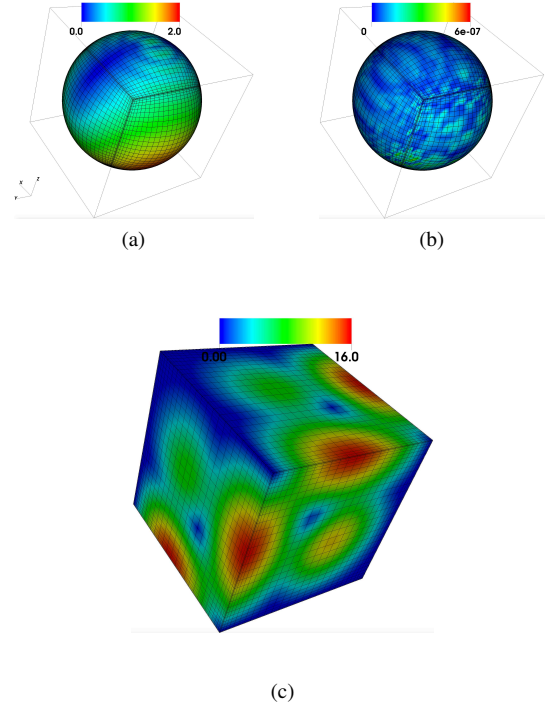


Fig. 4: (a) Surface current distribution on  $4\lambda$  diameter sphere. (b) Error in surface current distribution on  $4\lambda$  diameter sphere. The worst error is  $5.7 \times 10^{-7}$ . (c) Surface current distribution on  $1.2\lambda$  edge length cube.

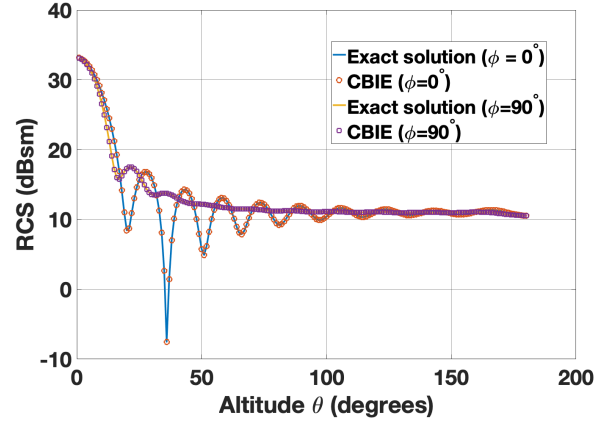


Fig. 5: Numerical vs exact RCSs corresponding to scattering of plane wave from  $D = 4\lambda$  PEC sphere at  $\phi = 0^\circ$  and  $\phi = 90^\circ$ .

permittivity  $\epsilon_d = 2\epsilon_e$  and a dielectric cube of  $2\lambda_e$  side length with permittivity  $\epsilon_d = 2\epsilon_e$ , where the  $\lambda_e = \frac{2\pi}{k_e}$  is the wavelength corresponding to the background exterior medium which is set to free-space for all problems considered here ( $\epsilon_e = \epsilon_0$ ). The permeability for both objects is also set to the vacuum permeability:  $\mu_d = \mu_e = \mu_0$ . The surfaces of the objects are discretized in the same manner as for the MFIE formulation, which results in  $Q = 2 \times 2 \times 6 \times N^2$  unknowns. They are both illuminated by a plane wave excitation  $\mathbf{E}^{\text{inc}} = \exp(-ikz) \hat{\mathbf{x}}$ . The results are compared against the Mie series analytical

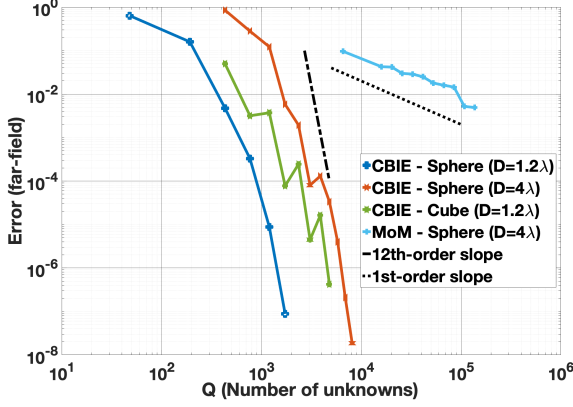


Fig. 6: Convergence of far-field error for the three scatterer examples vs number of unknowns. Performance of commercial MoM RWG-based solver is also plotted for  $D = 4\lambda$  sphere case for comparison. 2<sup>nd</sup> and 12<sup>th</sup> order asymptotes are drawn for reference.

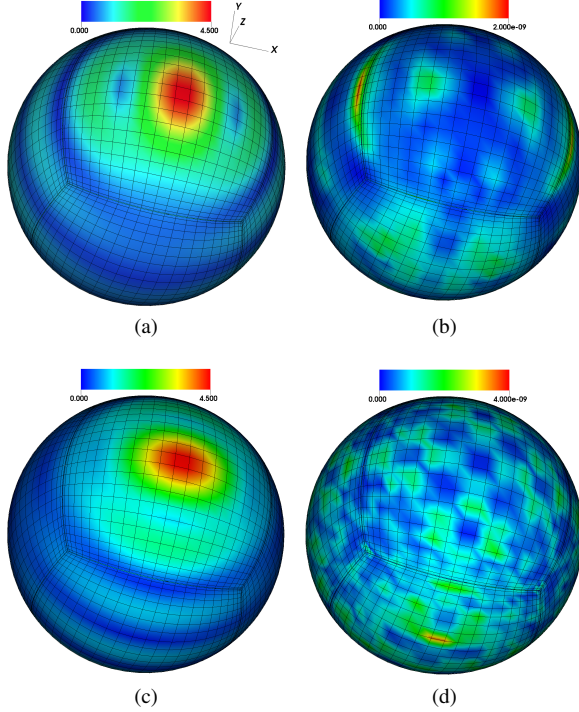


Fig. 7: (a) Surface  $J$  distribution on  $2\lambda_e$  diameter dielectric sphere with  $\epsilon_d = 2\epsilon_e$ . (b) Error of surface  $J$  distribution. Max error:  $1.9 \times 10^{-9}$ . (c) Surface  $M$  distribution. (d) Error of surface  $M$  distribution. Max error:  $3.5 \times 10^{-9}$ .

solution for the dielectric sphere [19] and against a highly refined numerical solution for the dielectric cube since an analytical solution does not exist.

Fig. 7(a) shows the electric ( $J$ ) current density distribution on the surface of the  $2\lambda_e$  sphere for  $N = 24$  and Fig. 7(b) shows the error difference of the computed electric current density distribution with the Mie Series solution. Fig. 7(c) and Fig. 7(d) show the magnetic ( $M$ ) current density distribution

and the corresponding error distribution respectively. It can be seen that the maximum relative error is smaller than  $3.5 \times 10^{-9}$  among all the discretization points on the sphere. Fig. 8 plots the computed RCS overlaid on top of the analytical far-field solution of the  $2\lambda$  sphere for varying altitudes at  $\phi = 0^\circ$  and  $\phi = 90^\circ$ .

Fig. 9 plots the error of the CBIE method vs number of unknowns ( $Q$ ) used to discretize each scatterer. As expected, the convergence for the cube is considerably worse than that of the sphere due to the edge and corner singularities which cause the surface densities to not be smooth. The convergence rate can be recovered, however, by using the same edge refinement approach proposed in [9] which clusters unknowns near the edges to better resolve the singularities. This improvement can be seen in the edge refined curve plotted in Fig. 9. As a comparison, the convergence of a commercial MoM RWG-based solver for the both objects is also plotted. For reference, 1<sup>st</sup> and 14<sup>th</sup> order slopes are drawn in dashed lines. As with the PEC case, the MoM solver only approaches first order convergence and requires a much finer discretization than the proposed CBIE method due to the linear basis functions and flat triangular discretization used to represent the geometry.

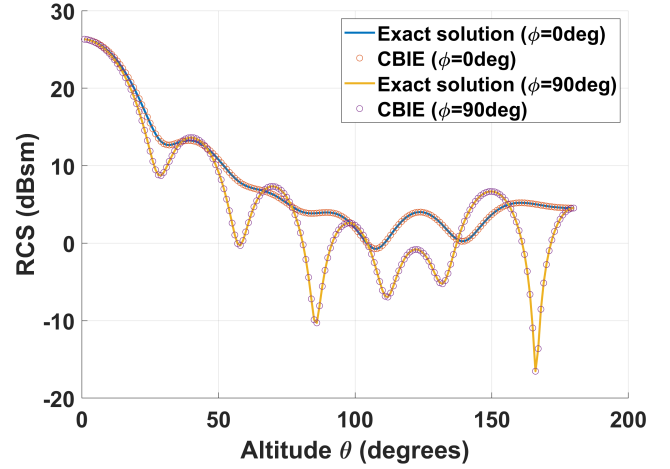


Fig. 8: Numerical vs exact RCSs corresponding to scattering of plane wave from  $D = 2\lambda_e$  dielectric sphere at  $\phi = 0^\circ$  and  $\phi = 90^\circ$ .

#### D. Scattering from complex NURBS CAD models

In order to demonstrate that the proposed approach can be readily used to solve scattering from complex CAD generated models with arbitrary curvature, we solve for the scattered fields from two different NURBS models freely available for download online [20]. As in the previous examples, the incident excitation is an  $x$ -polarized plane wave propagating in the  $+z$  direction. In the first example, we consider scattering off of a 16 wavelength tall humanoid bunny character. Fig. 10(a) shows the induced surface current density and Fig. 10(b) plots the RCS vs  $\theta$  at  $\phi = 90^\circ$  angle for two different discretizations ( $N = 10$  and  $N = 12$  Chebyshev points per side per patch or 100 and 144 points per patch total respectively). The model is comprised of 402 curvilinear quadrilateral patches total



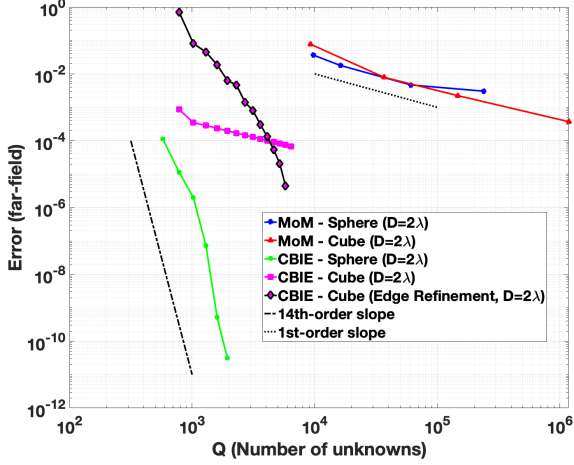


Fig. 9: Convergence of far-field error for the two dielectric scatterer examples vs number of unknowns. Convergence for the dielectric cube using edge refinement is also plotted. Performance of commercial MoM RWG-based solver is shown for comparison. 2<sup>nd</sup> and 14<sup>th</sup> order asymptotes are drawn for reference.

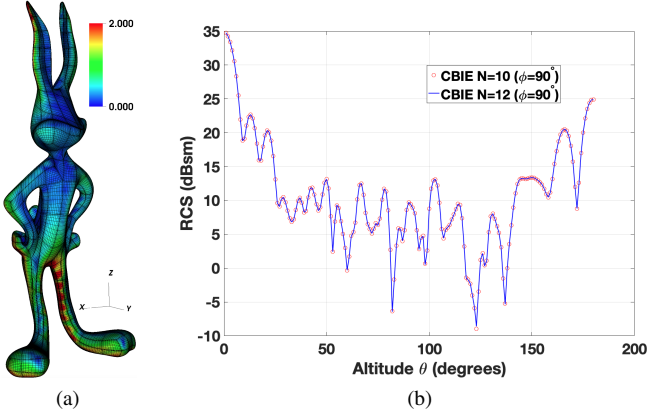


Fig. 10: (a) Surface electric current density induced on  $16\lambda$  tall PEC CAD humanoid bunny model by incident plane wave. The model consists of 402 curvilinear quadrilateral NURBS-parametrized patches. (b) RCS at  $\phi = 90^\circ$  corresponding to plane wave scattering for  $N = 10$  and  $N = 12$  Chebyshev points per patch discretizations.

and was directly imported from a standard CAD software without any special post-processing required [18]. Despite the large size of the model, significant variation in curvature, and regions with sharp corners (eg., the ears), the match in the RCS for the two relatively coarse discretizations is excellent and they are almost indistinguishable from one another, varying less than  $1 \times 10^{-4}$  from each other.

For the second CAD model example, we computed scattering from a glider with a length of 7.7 wavelengths and a wingspan of 5.6 wavelengths from the end of one wing to the other. Fig. 11(a) shows the induced surface current density and Fig. 11(b) plots the RCS vs  $\theta$  at  $\phi = 90^\circ$  angle for two

different discretizations ( $N = 10$  and  $N = 12$  Chebyshev points per side as before). The glider is comprised of 79 curvilinear quadrilateral patches total. As before, the RCS curves resulting from the two different discretizations match very well and vary less than  $2.5 \times 10^{-2}$  from each other.

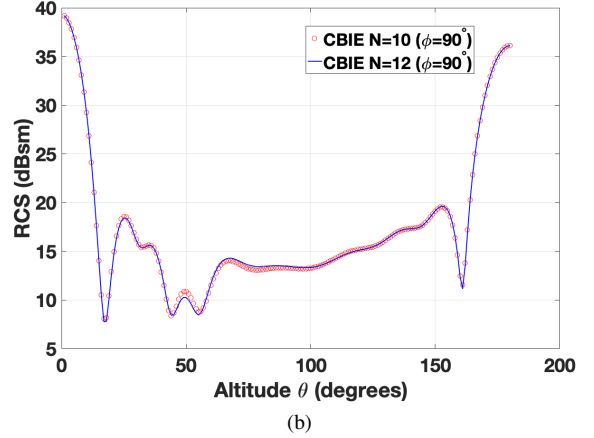
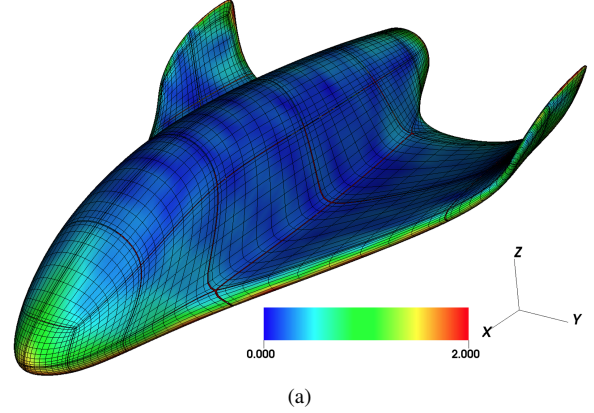


Fig. 11: (a) Surface electric current density induced on 79 patch PEC glider CAD model by incident plane wave. The glider spans 8 wavelengths from wing to wing. (b) RCS at  $\phi = 90^\circ$  corresponding to plane wave scattering for  $N = 10$  and  $N = 12$  Chebyshev points per patch discretizations.

## V. CONCLUSION

This paper presents a high-order accurate Chebyshev-based Boundary Integral Equation (CBIE) approach for solving Maxwell's equations. The CBIE method is applied towards the discretization of the MFIE and the N-Müller formulation. The performance is evaluated by solving scattering from sphere and cube PEC/dielectric objects and comparing against analytical solutions as well as a commercial MoM-based solver. We have also demonstrated a couple examples of scattering from complex 3D CAD models which contain many intricate features and variations in curvature. The proposed method achieves spectral convergence on sufficiently smooth surfaces with respect to the number of unknowns, significantly reducing the number of unknowns required for a desired accuracy over low-order MoM approaches. Furthermore, the CBIE approach also converges well for geometries with edges and corners when

an edge-refinement change of variables is utilized as demonstrated by the dielectric cube example. Current and future work involves applying the CBIE method in conjunction with the Windowed Green Function (WGF) [21] method towards the simulation and design of 3D waveguiding structures with unbounded boundaries for modeling nanophotonic devices [5], treating multi-material and composite objects [22]–[24], and incorporating acceleration techniques such as the Fast Multiple Method [25] or FFT-based methods [26], [27].

## REFERENCES

- [1] J. J. Bowman, T. B. Senior, and P. L. Uslenghi, “Electromagnetic and acoustic scattering by simple shapes (revised edition),” in *hpc*, 1987.
- [2] C. M. Lalau-Keraly, S. Bhargava, O. D. Miller, and E. Yablonovitch, “Adjoint shape optimization applied to electromagnetic design,” *Optics express*, vol. 21, no. 18, pp. 21 693–21 701, 2013.
- [3] A. Taflov and S. C. Hagness, *Computational electrodynamics: the finite-difference time-domain method*. Artech house, 2005.
- [4] O. C. Zienkiewicz, R. L. Taylor, P. Nithiarasu, and J. Zhu, *The finite element method*. McGraw-hill London, 1977, vol. 3.
- [5] C. Sideris, E. Garza, and O. P. Bruno, “Ultrafast simulation and optimization of nanophotonic devices with integral equation methods,” *ACS Photonics*, vol. 6, no. 12, pp. 3233–3240, 2019.
- [6] S. Rao, D. Wilton, and A. Glisson, “Electromagnetic scattering by surfaces of arbitrary shape,” *IEEE Transactions on antennas and propagation*, vol. 30, no. 3, pp. 409–418, 1982.
- [7] F. P. Andriulli, “Loop-star and loop-tree decompositions: Analysis and efficient algorithms,” *IEEE Transactions on Antennas and Propagation*, vol. 60, no. 5, pp. 2347–2356, 2012.
- [8] O. Bruno, T. Elling, R. Paffenroth, and C. Turc, “Electromagnetic integral equations requiring small numbers of krylov-subspace iterations,” *Journal of Computational Physics*, vol. 228, no. 17, pp. 6169–6183, 2009.
- [9] O. P. Bruno and E. Garza, “A chebyshev-based rectangular-polar integral solver for scattering by general geometries described by non-overlapping patches,” *arXiv preprint arXiv:1807.01813*, 2018.
- [10] A. Maue, “On the formulation of a general scattering problem by means of an integral equation,” *Z. Phys*, vol. 126, no. 7, pp. 601–618, 1949.
- [11] C. Müller, *Foundations of the mathematical theory of electromagnetic waves*. Springer Science & Business Media, 2013, vol. 155.
- [12] P. Ylä-Oijala, M. Taskinen, and S. Järvenpää, “Analysis of surface integral equations in electromagnetic scattering and radiation problems,” *Engineering Analysis with Boundary Elements*, vol. 32, no. 3, pp. 196–209, 2008.
- [13] J. Volakis, *Integral equation methods for electromagnetics*. The Institution of Engineering and Technology, 2012.
- [14] P. Yla-Oijala and M. Taskinen, “Well-conditioned muller formulation for electromagnetic scattering by dielectric objects,” *IEEE Transactions on Antennas and Propagation*, vol. 53, no. 10, pp. 3316–3323, 2005.
- [15] J. C. Mason and D. C. Handscomb, *Chebyshev polynomials*. CRC press, 2002.
- [16] D. L. Colton, R. Kress, and R. Kress, *Inverse acoustic and electromagnetic scattering theory*. Springer, 1998, vol. 93.
- [17] J. Kiefer, “Sequential minimax search for a maximum,” *Proceedings of the American mathematical society*, vol. 4, no. 3, pp. 502–506, 1953.
- [18] Robert McNeel & Associates, “Rhino3d,” [Online]. Available: <https://www.rhino3d.com/>
- [19] R. F. Harrington, “Time-harmonic electromagnetic fields,” 2001.
- [20] “GrabCAD,” [Online]. Available: <https://grabcad.com/>
- [21] O. P. Bruno, E. Garza, and C. Pérez-Arancibia, “Windowed green function method for nonuniform open-waveguide problems,” *IEEE Transactions on Antennas and Propagation*, vol. 65, no. 9, pp. 4684–4692, 2017.
- [22] P. Yla-Oijala, M. Taskinen, and J. Sarvas, “Surface integral equation method for general composite metallic and dielectric structures with junctions,” *Progress In Electromagnetics Research*, vol. 52, pp. 81–108, 2005.
- [23] C. Pérez-Arancibia, C. Turc, L. Faria, and C. Sideris, “Planewave density interpolation methods for the efie on simple and composite surfaces,” *arXiv preprint arXiv:1910.02046*, 2019.
- [24] C. Pérez-Arancibia, C. Turc, and L. Faria, “Planewave density interpolation methods for 3d helmholtz boundary integral equations,” *SIAM Journal on Scientific Computing*, vol. 41, no. 4, pp. A2088–A2116, 2019.
- [25] N. Engheta, W. D. Murphy, V. Rokhlin, and M. S. Vassiliou, “The fast multipole method (fmm) for electromagnetic scattering problems,” *IEEE Transactions on Antennas and Propagation*, vol. 40, no. 6, pp. 634–641, 1992.
- [26] O. P. Bruno and L. A. Kunyansky, “A fast, high-order algorithm for the solution of surface scattering problems: basic implementation, tests, and applications,” *Journal of Computational Physics*, vol. 169, no. 1, pp. 80–110, 2001.
- [27] E. Bleszynski, M. Bleszynski, and T. Jaroszewicz, “Aim: Adaptive integral method for solving large-scale electromagnetic scattering and radiation problems,” *Radio Science*, vol. 31, no. 5, pp. 1225–1251, 1996.